Combining Borrmann and weak-beam diffraction images to study defects in a high-quality CdTe(Zn) crystal

T. Journot, D. Brellier, P. Ballet, T. N. Tran Thi Caliste, E. Gout, D. Collonge, J. Baruchel

HAL Id: cea-04057392

https://cea.hal.science/cea-04057392

Submitted on 4 Apr 2023

Combining Borrmann and weak-beam diffraction images to study defects in a high-quality CdTe(Zn) crystal

T. Journot, D. Brellier, P. Ballet, T. N. Tran Thi Caliste, E. Gout, D. Collonge and J. Baruchel

IUCr Journals
CRYSTALLOGRAPHY JOURNALS ONLINE

Combining Borrmann and weak-beam diffraction images to study defects in a high-quality CdTe(Zn) crystal

T. Journot,[a]* D. Brellier,[a] P. Ballet,[a] T. N. Tran Thi Caliste,[b] E. Gout,[a] D. Collonge[a] and J. Baruchel[b]

Edited by A. Borbély, Ecole National Supérieure des Mines, Saint-Etienne, France

[a]Grenoble Alpes University, CEA-LETI, 17 Avenue des Martyrs, F-38054 Grenoble, France, and [b]European Synchrotron Radiation Facility, 71 Avenue des Martyrs, F-38043 Grenoble, France. *Correspondence e-mail: timotee.journot@cea.fr

In this work, synchrotron radiation rocking curve imaging (RCI) is used to visualize and characterize dislocations and second-phase defects in a highly perfect and absorbing CdTe(Zn) crystal. This technique requires recording a series of Bragg diffracted images along the rocking curve to produce maps of the 'local' integrated intensity, full width at half-maximum and peak position. The diffraction conditions of the reported experiment are such that anomalous transmission (Borrmann effect) is a crucial ingredient for the formation of the image of the defects. The images recorded and maps produced allow the investigation of a series of topics that, to the authors' knowledge, have not been previously studied. The first of these topics is the variation of the position and width of the Borrmann image of a defect when sitting on the peak and on the flanks of the diffraction curve. The second topic is the way Borrmann images show up on the usual RCI maps. The final topic is the combination of Borrmann and weak-beam images to infer the depth of the defect within the crystal.

1. Introduction

Anomalous transmission (Borrmann effect) is a dynamical-theory-related effect that can be observed when a highly perfect and absorbing crystal (high μt value, where μ is the absorption coefficient of the material and t the thickness of the sample) is set for Bragg diffraction (Borrmann, 1941). For work on general dynamical theory, see Authier (2004). This effect is observed when μt is typically >8–10, but can also be produced for slightly lower values of μt. For such high-absorption conditions, the incident radiation is nearly completely absorbed except for wavefields belonging to the centre of the perfect-crystal reflection range. The electric field of these wavefields approaches zero amplitude at the crystal planes, thus dramatically reducing the photoelectric absorption. The wavefields affected by this anomalous absorption are those associated with one of the branches of the dispersion surface, which undergo a reduced absorption, whereas those associated with the other branch are, conversely, preferentially absorbed (*e.g.* Authier, 2004). As a consequence, within a very narrow incidence angular range (on the order of 1 arcsecond), a transmitted beam (forward diffracted) and a diffracted beam appear behind the crystal. The energy flow (Poynting vector), inside the crystal, of the wavefields involved in the anomalous transmission is directed along the lattice planes involved in Bragg diffraction. Each of these wavefields splits at the exit surface into diffracted and transmitted waves. In the usual case (as in Fig. 1), the detector is set to record the diffracted beam, but the 'forward diffracted' beam can also be recorded.
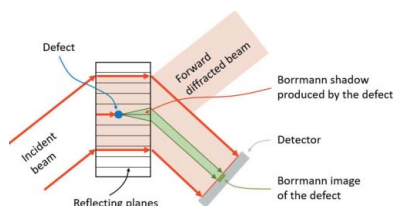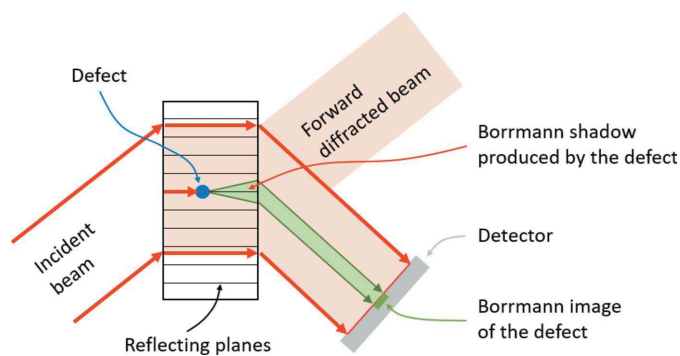
Figure 1
Schematic to show the propagation of the wavefields that undergo anomalous transmission, and the Borrmann shadow introduced by a defect (see text).

Lattice defects 'disturb' the anomalous transmission. When the strain gradient around the defect is high, new wavefields are created and propagate. Most of these new wavefields are strongly absorbed, and this leads to a locally reduced intensity (Borrmann shadow, as shown schematically in Fig. 1). The width of the shadow at the exit surface is proportional to the distance of the defect from the surface. The contrast of the defects is therefore higher when they are close to the exit surface because less of the Borrmann diffracted intensity that propagates outside the defect reaches the area corresponding to the intersection of the Borrmann shadow triangle with the exit surface. The centre of the Borrmann image at the peak of the rocking curve corresponds to the projection of the defect on the exit surface along the direction parallel to the lattice planes (Klapper, 1996). As an example, the Borrmann image of a dislocation on a section topograph is described in Appendix A.

The value of the intrinsic width of the diffraction curve for a perfect crystal given by the dynamical theory of diffraction is, typically, in the few-microradians range. If a defect is present in such a crystal, an image recorded on the tail of the rocking curve under nearly plane wave diffraction conditions predominantly shows the image of the distorted area surrounding this defect that is in Bragg diffraction for this angular position. This image is known as the weak-beam image of the defect. Weak-beam images, which are often used in monochromatic synchrotron radiation diffraction topography (Sauvage, 1980; Baruchel, 1996; Tanner, 1996), are difficult to visualize under high-absorption conditions because they do not contribute to the anomalous transmission. However, they nevertheless arise and are observable if (i) the absorption, while high, allows some transmission and (ii) the intensity of the incident beam and the signal-to-noise ratio (SNR) of the detector are sufficiently high. This appears to be the case for the experiment reported here.

CdTe(Zn) is considered to be the ideal substrate for HgCdTe epitaxy, owing to the possibility of adapting the lattice constant of the substrate to that of the layer by varying the Zn concentration (Capper, 1994; Basson & Booyens, 1983; Takigawa et al., 1988). The high crystalline quality of HgCdTe required to produce high-performance infrared sensors is directly linked to the defect concentrations in the CdTe(Zn) substrate (Yildirim et al., 2021). Therefore, it is of major concern to reduce both the dislocation density and the second-phase defects in CdTe(Zn), since they are at the origin of the crystal quality degradation of the HgCdTe active layers.

The existing conventional characterization techniques to investigate dislocations in CdTe(Zn) crystals are mostly destructive or indirect. Dedicated chemical etching reveals the emerging dislocations on the surface of the substrate. However, no description of either the dislocation type or their volumetric arrangement can be obtained. The same is true for typical X-ray rocking curve analyses, which can only provide some indirect information about dislocations. Transmission electron microscopy (TEM) can directly detect the spatial distribution of dislocations with real and reciprocal space information owing to the adjustable objective lenses (Williams & Carter, 1996). However, the information obtained by TEM is limited to a small area and, thus, may not be representative of the entire sample. Moreover, aside from being a destructive method, studying dislocations in CdTe(Zn) samples with typical dislocation densities below $10^4 \, \mathrm{cm}^{-2}$ by TEM is challenging. Therefore, we need a nondestructive method that can characterize the whole volume of a sample in a representative manner combined with high angular resolution, and can also probe the strain fields around defects. X-ray Bragg diffraction topography offers an interesting option for overcoming the above-mentioned difficulties.

In the present work we use the rocking curve imaging (RCI) (Lübbert et al., 2000) technique to visualize and characterize defects (dislocations, second-phase defects) in a highly perfect and highly absorbing CdTe(Zn) crystal. This technique requires the recording of a series of images at different angular locations of the diffraction rocking curve. These images allowed the investigation of a series of topics that, to the best of our knowledge, have not been studied previously. The first of these topics is the variation of the Borrmann effect on the peak, flanks and tails of the diffraction curve. The second topic is the way Borrmann images show up on the usual RCI maps: (i) integrated intensity, (ii) full width at half-maximum (FWHM) and (iii) peak position. The FWHM is the width of the Gaussian that best fits the rocking curve recorded on a given pixel of the detector, and the peak position is the centre of this Gaussian. The final topic is the combination of Borrmann and weak-beam images to infer the depth of the defect within the crystal.

2. Sample and experimental technique

The experiment was carried out at beamline BM05 of the ESRF on a (111)-oriented (offcut < 0.2°), platelet-shaped CdTe(Zn) crystal containing 2 at.% Zn, grown by the vertical-gradient freeze technique (Brellier et al., 2014) with the growth axis parallel to [111]. The dimensions of the studied sample are $30 \times 30 \times 0.5$ mm. It was extracted from a 115 mm-diameter single crystal grown at the CEA, Grenoble. The quality of this single crystal, while globally high, was not uniform, and displayed millimetre-sized very high quality

areas where the dislocation density was as low as ∼500 cm^{-2}. All the images shown in this article were taken in these areas. Elsewhere, in the more defective zones, the dislocation density can increase by two orders of magnitude. More details about the growth and the defects observed in these crystals will be published elsewhere. To produce the diffraction images, we used the 220 reflection in transmission geometry at 20 keV ($\theta_B = 7.8°$, $\mu t \simeq 6$).

RCI is a quantitative version of monochromatic Bragg diffraction topography with spatial resolution and angular resolution nowadays obtainable in the micrometre and microradian ranges, respectively (Mikulík *et al.*, 2006; Tsoutsouva *et al.*, 2015; Tran Thi Caliste *et al.*, 2021). RCI is performed using a monochromatic beam originating from an Si(111) double-crystal monochromator (with a third-harmonic contamination more than 10^3 times smaller than the first-harmonic beam for our experimental conditions), and recording a series of images (100 in the present work with an angular step of 10$^{-4°}$) at different consecutive angular positions by rocking around the Bragg angle along the Bragg diffraction rocking curve. The diffracted-beam images are recorded on a two-dimensional pixelated detector with an effective pixel size of 0.6 × 0.6 μm^2 (leading to a field of view of ∼1.2 × 1.2 mm^2) positioned approximately 160 mm downstream of the sample and perpendicular to the diffracted beam.

The data recorded along the rocking curve are processed and analysed pixel-by-pixel using purpose-developed software (https://gitlab.com/l_sim/scripts/rcia). Maps of the 'local' integrated intensity, FWHM and peak position are then generated from the rocking curves recorded on each pixel. The last two maps result from a Gaussian fit of the rocking curve recorded on each individual pixel. This fit has proved to be a good approximation for the rocking curves we measure, which result from a convolution of the intrinsic width of the rocking curve with experimental and defect-related angular spreads. The peak position maps presented are corrected to eliminate the dispersion associated with the monochromator (Servidori *et al.*, 2001). As the quality of our crystal was very high, we recorded a single rocking curve, not a composite one, on each of the pixels. All the maps shown in the present work are displayed in such a way that the projection of the diffraction vector is vertical, and the intensity and/or angular scales are linear.

3. Results

3.1. Borrmann images and their variation along the rocking curve

Fig. 2 shows a Bragg diffraction image (topograph) recorded at the maximum-intensity peak of the rocking curve. We can observe, on this topograph, images of dislocations (lines) and second-phase defects (dots). These images display a lower intensity than the matrix, resulting from the anomalous transmission and the associated Borrmann shadow described above. We point out, more specifically, the images of four dislocations (D_1, D_2, D_3, D_4) and two second-phase

defects (S_A, S_B), which exhibit a lower intensity than the dislocations. A given dislocation image displays a rather constant width over large portions of the image, *i.e.* the Borrmann shadow produced is also constant for the portion of the dislocation considered, suggesting that this portion of the dislocation is nearly parallel to the surface. Nevertheless, the widths of the various dislocation images are different (∼15 μm
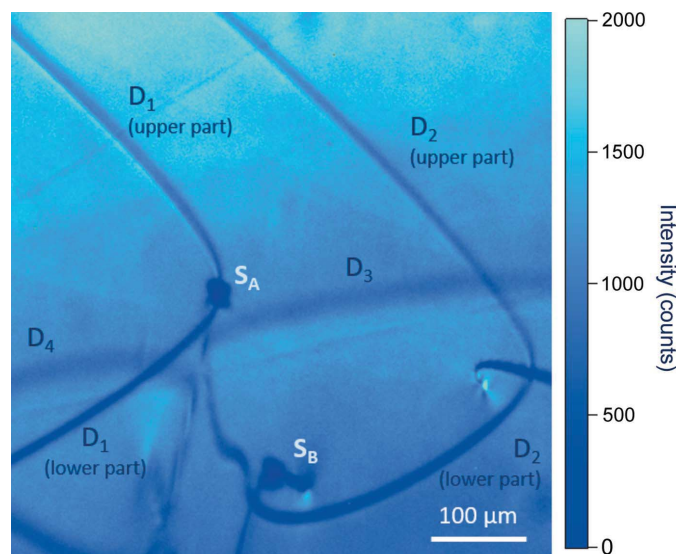

Figure 2
Topograph recorded at the maximum of the rocking curve. It shows images of dislocations (D_1 to D_4) and second-phase defects (S_A and S_B). The sharpness of the images indicates the defect distance from the exit surface: sharp close to the surface, diffuse away from it. The projection of the diffraction vector is vertical for all the topographs and maps shown in the present work.
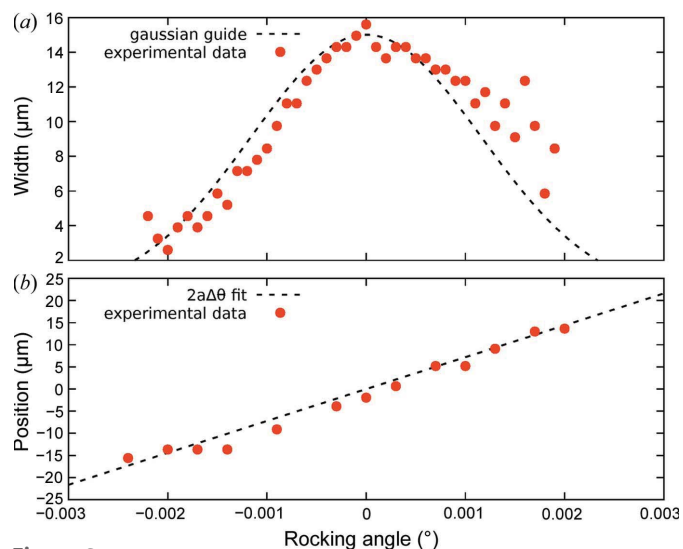
Figure 3
(*a*) Width of a dislocation image (in μm) and (*b*) variation of the position of the centre of the image of a dislocation with respect to this position at the peak of the rocking curve (in μm), as a function of the angular position on the rocking curve. The Gaussian fit is intended to be a guide for the eye. The positions of the centre of the image measured in (*b*) are consistent with the diffraction geometry as the Bragg angle is changed (see the *Discussion*). The $2a\Delta\theta$ linear function (with $a = 160$ mm) fits the experimental data well.
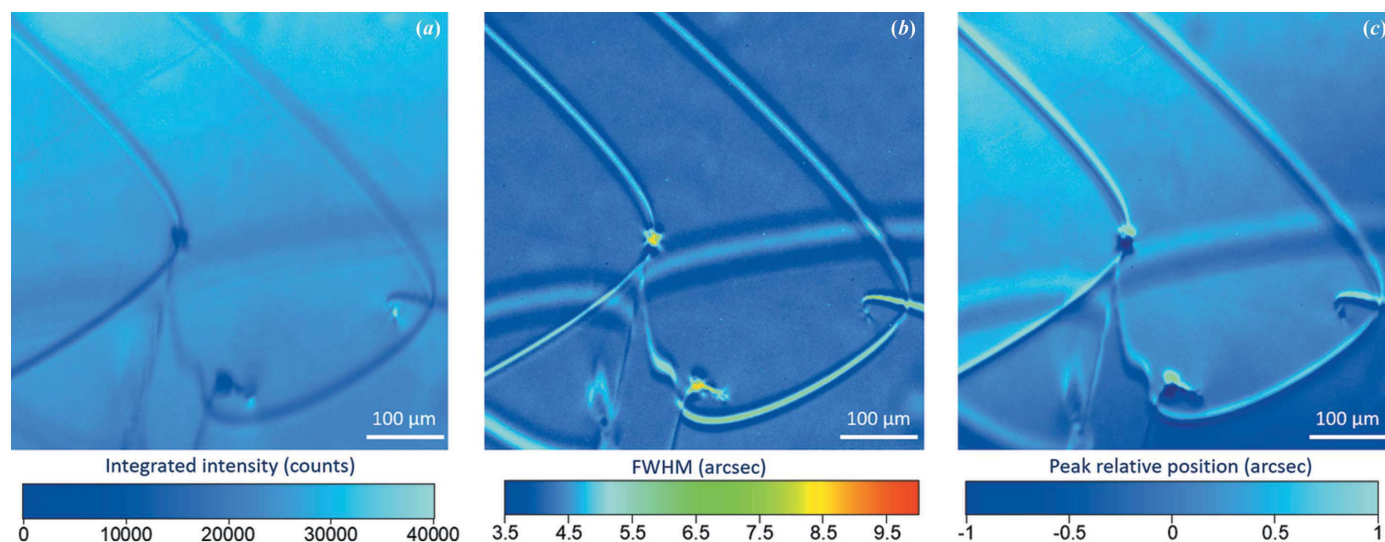
Figure 4
RCI maps of the region of the crystal imaged in Fig. 2, extracted from the rocking curves recorded on each of the pixels of the detector: (a) integrated intensity map (b) FWHM map (c) peak position map.

for D_1 and D_2, ~30 μm for D_3 and D_4), indicating that their distance from the exit surface is different: D_1 and D_2 appear to be closer to the exit surface than D_3 and D_4. We will discuss this point in more detail in Section 4.3.

Fig. 3 shows the experimental evolution of the width [Fig. 3(a)] and the central position [Fig. 3(b)] of a dislocation image, as measured on the topographs recorded on the peak and flanks of the rocking curve. We note that (i) the width of the dislocation image is maximum at the peak, and reduces

when moving away from this angular position; and (ii) the centre of the dislocation image evolves as a function of the angular position on the rocking curve.

3.2. Borrmann images in the integrated intensity, FWHM and peak position maps

Fig. 4(a) shows the RCI integrated intensity map of the same region as that imaged on the peak of the rocking curve in Fig. 2. These two images display very similar features. This is
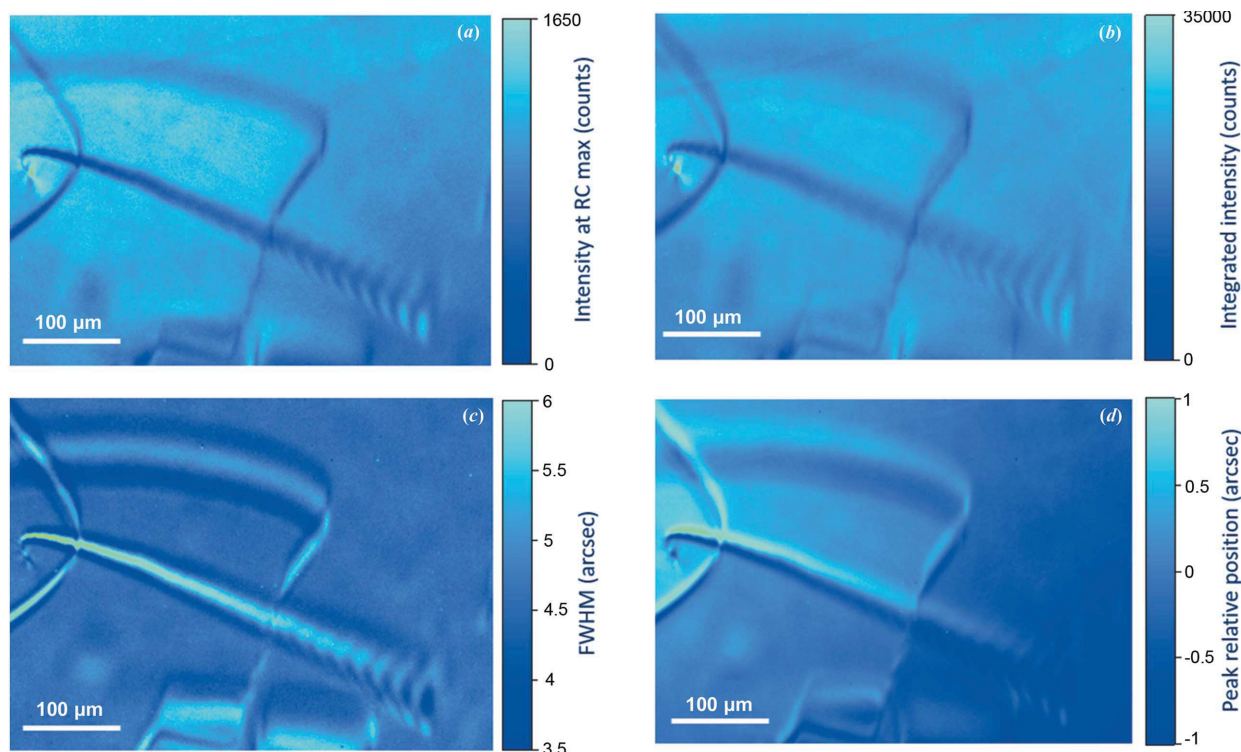

Figure 5
(a) Topograph at the peak of the rocking curve and RCI maps [(b) integrated intensity, (c) FWHM and (d) peak position] showing a threading dislocation, going from one surface to the other of the crystal in the Borrmann case studied here.

not surprising because the image on the peak constitutes a major contribution to the integrated intensity map. Note that, in both Figs. 2 and 4(a), the lower-intensity images of the dislocations are surrounded by thin lines of slightly (<10%) higher intensity than the matrix.

The corresponding FWHM map [Fig. 4(b)] shows that the area corresponding to the integrated intensity map Borrmann image exhibits a higher value of the FWHM (5 arcseconds compared with ~4 arcseconds for the perfect crystal matrix, both values corresponding, as already indicated, to a convolution with an experimental angular spread). It also shows that this 'higher value FWHM' image is surrounded, on both sides, by a region of apparent smaller FWHM, which appears to correspond to the lines of slightly higher intensity on the peak position map and rocking curve peak topograph. This last feature is probably not related to the high absorption, because it was already observed in the low-absorption case on high-quality diamonds, as will be discussed in Section 4.

Fig. 4(c) shows the peak position map of the same region of the crystal, which qualitatively behaves like those observed in the low-absorption case: it displays a peak position variation of about of ~1 arcsecond on going from one side to the other of the dislocation (and second-phase defect) centre of the image (Tsoutsouva et al., 2015). In addition, note that the peak position map [Fig. 4(c)] shows that there is a faint curvature of the sample (radius of curvature ~200 m) on going from the left side to the right side of the image. As the crystalline matrix around the various dislocations is slightly rotated (in the microradian range), the relative angular position of the dislocations is also slightly rotated, within the same range.

Fig. 5 shows the images of threading dislocations that run from one surface to the other. They display a variable width: large near the entrance surface and narrow near the exit surface. In addition, these images exhibit interference fringes as observed, for instance, in GaAs with similar absorption conditions by Tanner (1996).

The FWHM and peak position maps show the features that were already observed for dislocations parallel to the surface.

These maps show, in particular, that the fringes display a higher FWHM where the intensity is lower. These fringes are associated with the high crystalline quality of the crystal, and show up, in a similar way, in the low-absorption case.

3.3. Combining Borrmann and weak-beam images to infer the depth of the defect

Fig. 6(a) shows, again, the topograph from Fig. 2, recorded at the top of the rocking curve, where the Borrmann images of dislocations are visible. The weak-beam images of the same dislocations are observable on the tails of the rocking curve [Fig. 6(c)]. The experiment reveals that there are some angular positions on the rocking curve where Borrmann and weak-beam images are simultaneously visible [Fig. 6(b)]. These images show that the Borrmann and weak-beam images do not appear at the same location on the detector.

Let us recall that the centre of the Borrmann images is, in the case of Fig. 6(b), displaced with respect to the one at the peak of the rocking curve, as indicated by the curve shown in Fig. 3(b). We consider that the location of the Borrmann image is the one corresponding to the centre of this image for the topograph recorded on the peak of the rocking curve. In the next section, we explain how the variation of positions between the Borrmann images on the peak and the weak-beam images on the tail of the rocking curve enable the calculation of the distance to the exit surface of the dislocation considered.

4. Discussion

4.1. Borrmann images as a function of the position on the rocking curve

The Borrmann images observed on the peak of the rocking curve are in agreement with previously published work (e.g. Klapper, 1996; Authier et al., 1985; Suvorov et al., 2007; Suvorov & Smirnova, 2015).

Fig. 3 shows that the position of the centre of the Borrmann image of a dislocation varies as a function of the angular
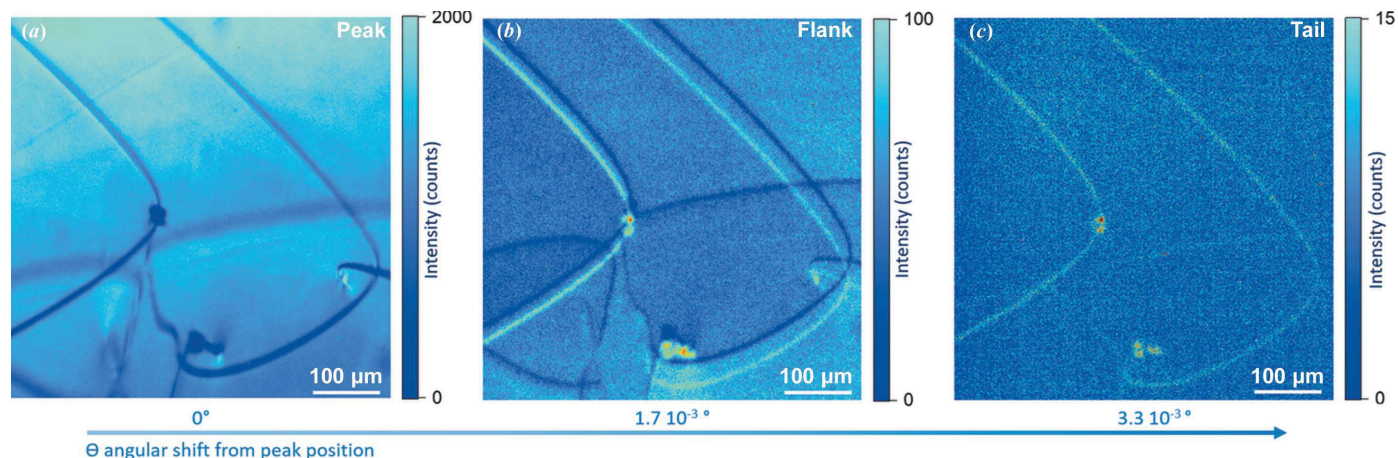

Figure 6
Topographs recorded (a) on the peak of the rocking curve, which shows the Borrmann images of dislocations and second-phase defects, (b) on the flank of the rocking curve, which enables the simultaneous visualization of Borrmann and weak-beam images of the defects, and (c) on the tail of the rocking curve, which only shows the weak-beam images.

position on the rocking curve of the recorded image. It also shows that the width of this image is reduced on the flanks with respect to that observed on the peak of the rocking curve.

When sitting on the flank of the rocking curve, the wavefields that propagate under anomalous transmission conditions are partly associated with the divergence and wavelength spread ($\Delta\lambda/\lambda \simeq 10^{-4}$) produced by the Si(111) double-crystal monochromator. This component of the incoming beam produces wavefields that also propagate along the reflecting planes, and, outside of the crystal, lead to diffracted beams that reach the detector at a distance x from the centre of the image on the peak such that $x = 2a\Delta\theta$, where a is the crystal-to-detector distance and $\Delta\theta$ is the departure angle from the centre of the rocking curve. This leads to $x = 11$ μm for an angle $\Delta\theta = 2 \times 10^{-3\circ}$, in good agreement with the experimental results shown in Fig. 3(b).

Fig. 3(a) shows that the width of the Borrmann image on the flanks of the rocking curve is smaller than that at the peak. This indicates that the Borrmann shadow is angularly reduced when we move away from the peak position. Note that the width of the dislocation image at the peak of the rocking curve and the displacement of its centre for the various angular locations on this rocking curve are both in the 10 μm range. The width of the image of the dislocation at the peak of the rocking curve corresponds to wavefields produced after the dislocation that propagate within the Borrmann shadow triangle. This suggests that, when moving away from the peak along the rocking curve, only a fraction of these wavefields are produced, and only a part of the image at the peak is visible. The displacement of the centre of the image and the width of the image at the peak are therefore, within this qualitative approach, expected to be of the same order. This appears to be in fair agreement with the measured values in Fig. 3: the apparent width of the investigated dislocation image at the peak of the rocking curve is ~16 μm, and the displacement of the centre of the dislocation image is about ±11 μm. This last fact could correspond to the high SNR of the detected image, which enables us still to measure a faint Borrmann image of the dislocation far from the peak of the rocking curve.

4.2. RCI maps

The various RCI maps allow the visualization and characterization of the defects. What we observe from the FWHM and the peak position maps are the features corresponding to the neighbourhood of the defect. These maps suggest that the new wavefields that are produced after the defect and propagate within the Borrmann shadow 'transport' to the exit surface the local FWHM and peak position that are present around the defect.

The integrated intensity map [Fig. 4(a)] shows the dislocation images associated with the Borrmann effect: the measured intensity within these images is, for dislocations D_1 and D_2, less than 1/3 of the intensity measured for the matrix. An additional observation of these dislocation images shows the occurrence of faint 'accompanying lines', with intensity ~7% higher than that of the matrix. On the FWHM map [Fig. 4(b)] the Borrmann images of the dislocations appear as lines that display a measured FWHM ~20% higher than the matrix, and the accompanying lines as lines of an apparently smaller FWHM (~10%) than the matrix. Note that all the measured FWHMs result from a convolution, and therefore these percentages are only indicative. The accompanying lines (higher apparent intensity in the integrated intensity map/ lower apparent FWHM in the FWHM map) observed on these maps are reminiscent of the dynamical-theory-related interference fringes leading to lower FWHM when the intensity is higher. These fringes were observed in several high-quality (and low-absorption; $\mu t \simeq 0.8$) diamond crystals, in particular in the work of Tran Thi Caliste *et al.* (2023), where the dynamical theory calculations are compared with the experimental results on Kato fringes. This previous work suggests a similar origin for the fringes we observe here, for the case where $\mu t \simeq 6$.

4.3. Borrmann and weak-beam images

Note that the weak-beam images, recorded on the tails of the rocking curve, do not undergo anomalous absorption. They are therefore observed because the absorption of our sample, albeit strong, allows a detectable transmitted beam (a simple calculation indicates that the reduction in the intensity of this beam is ~10^3), and because both the beam intensity and the SNR of the detector are sufficiently high. Fig. 6(c) shows that our detector is able to discriminate a weak-beam signal of ten counts over a background of about five counts, with an exposure time of 10 s.

The weak-beam image of a dislocation (with intensity higher than that of the matrix, which is not in the Bragg position) corresponds to the projection, along the diffracted direction, of the intersection of the dislocation with the incoming beam (similar to the 'direct image' contrast mechanism; Authier, 2004). A weak-beam image of a second-phase defect contains two higher-intensity spots aligned along the diffraction vector. They correspond to the projection, along the diffracted direction, of the distorted zones around the core of the defect which are simultaneously in the Bragg position (while the matrix is not). Examples of these weak-beam signals from dislocations and second-phase defects are visible in Fig. 6(c).

Fig. 7 is a schematic showing the simple case of a horizontal dislocation (blue dot) parallel to the main surfaces, *i.e.* perpendicular to the plane of the drawing. This case is not purely academic because it corresponds to many of the dislocations we observe in our sample, and also to second-phase defects.

A very simple relation relates distance d on the detector (perpendicular to the diffracted beam), between the centre of the Borrmann image and the weak-beam image of the same dislocation, and distance p to the exit surface of the dislocation:

$$p = d/\sin\theta_B.$$

From the measurement of the variation of position d between the Borrmann images on the peak and the weak-beam images

on the tail of the rocking curve, we can subsequently calculate the distance p to the exit surface of each of the dislocations that are parallel to the surface, as well as that of the observed second-phase defects. When the dislocations are not parallel to the surface, the same formula applies for each of the points of the dislocation, and allows to us follow the variation of depth with respect to the surface. As mentioned before, for the second-phase defects, the weak-beam signal is doubled and originates from the distortion field around the core of the defect. Then, to estimate its depth, the average position of the two hot spots that constitutes the weak-beam signal of the defect must be used. For the second-phase defects and dislocations indicated in Fig. 2, we obtain the values in Table 1.

This analysis shows that the second-phase defect S_A and the dislocation D_1, which appear at the same location when looking at the projection maps (*cf*. Figs. 2 and 4), seem to be connected. Their distances to the exit surface (p) are similar, and the second-phase defect seems to act as an anchor point for the dislocation D_1, which is bent. The same remarks apply for D_2 and its possible interaction with S_B and the dislocation travelling from surface to surface on the right-hand side of Fig. 2. Generally speaking, Fig. 2 suggests that dislocations interact with other material defects as they are found to change direction in the vicinity of a defect, whether it is a second-phase defect or another dislocation. However, in defect-free areas, dislocations follow straight paths.

These results also enable the estimation of the angle (2α) of the Borrmann shadow triangle, which is, for a dislocation, such that $\tan \alpha = w/2p$, where w is the width of the dislocation image on the peak of the rocking curve and p is the distance of the dislocation with respect to the exit surface. This leads to an average estimation $2\alpha \simeq 6°$ for the Borrmann shadow angle, *i.e.* roughly more than $2\times$ smaller than the top angle $2\theta_B$ of the Borrmann prism. This measured ratio provides some information about the excitation of new wavefields across the dispersion surface below the defect. A more quantitative
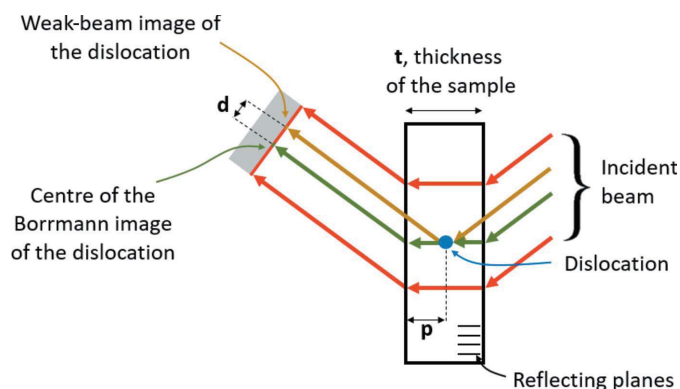

Figure 7
Schematic that considers the case of a dislocation line horizontal and parallel to the main surfaces, *i.e.* perpendicular to the plane of the drawing. In this case, the three-dimensional problem involving the Borrmann prism (which has, as its base, the Borrmann triangle, and the length of the horizontal extension of the beam as height) reduces to a two-dimensional problem. The drawing allows the extraction of a very simple relationship between d, the distance on the detector between the Borrmann and weak-beam images of the dislocation, and p, the distance to the exit surface.

Table 1
The d and p distances of the defects (dislocations and second-phase defects) from Fig. 2.

Defect	d (μm) ± 1 μm	p (μm) ± 8 μm
D_1 upper part	9	68
D_1 lower part	14	104
D_2 upper part	28	210
D_2 lower part	32	240
D_3	60	454
S_A	10	75
S_B	15	115

analysis should take into account the wavelength of the X-rays, as well as the crystal structure and the thickness.

5. Conclusions

The availability of a highly perfect crystal of CdTe(Zn) grown at the CEA-LETI enabled us to carry out an investigation of the way dislocations and second-phase defects show up under anomalous transmission conditions. This has never been performed before because both highly perfect crystals of CdTe(Zn) and a performant RCI-devoted device were not available. The present work also enabled us to acquire a better knowledge of the images of these defects on the usual RCI maps, which is important for the accurate interpretation of the maps recorded for a series of similar crystals. Finally, the fact that we can observe not only the Borrmann image of a defect but also its weak-beam image enables extraction of the depth of this defect with respect to the exit surface. The calculated depths are in agreement with those estimated from the width of the Borrmann shadow images.

RCI is a powerful tool to characterize dislocations in CdTe(Zn)-based crystals that supplements the commonly used conventional techniques. The visualization of the dislocation network inside the crystals enabled by RCI is important to go further in the understanding of these defects (mechanisms of formation, of propagation, of interaction with other defects *etc.*). This understanding could provide clues to improve the crystallization process of CdTe(Zn)-based alloys.

APPENDIX *A*
Borrmann image of a dislocation on a section topograph

In the case of section topographs, it is known (Klapper, 1996) that the centre of the Borrmann image of the dislocation, with lower intensity than the matrix, corresponds to the projection [in light blue in Fig. 8(*a*)] on the exit surface, along the reflecting plane direction, of the part of the dislocation present within the Borrmann prism ABCDEF, as indicated in the schematic of Fig. 8 (Klapper, 1996; Authier *et al.*, 1985; Suvorov *et al.*, 2007; Suvorov & Smirnova, 2015).

A section topograph (Fig. 8) was recorded on the sample used in this work. The 10 μm-thick incident beam crosses the path of the lower part, in Fig. 2, of the dislocations D_1 and D_2, which are nearly parallel and close to the exit surface.
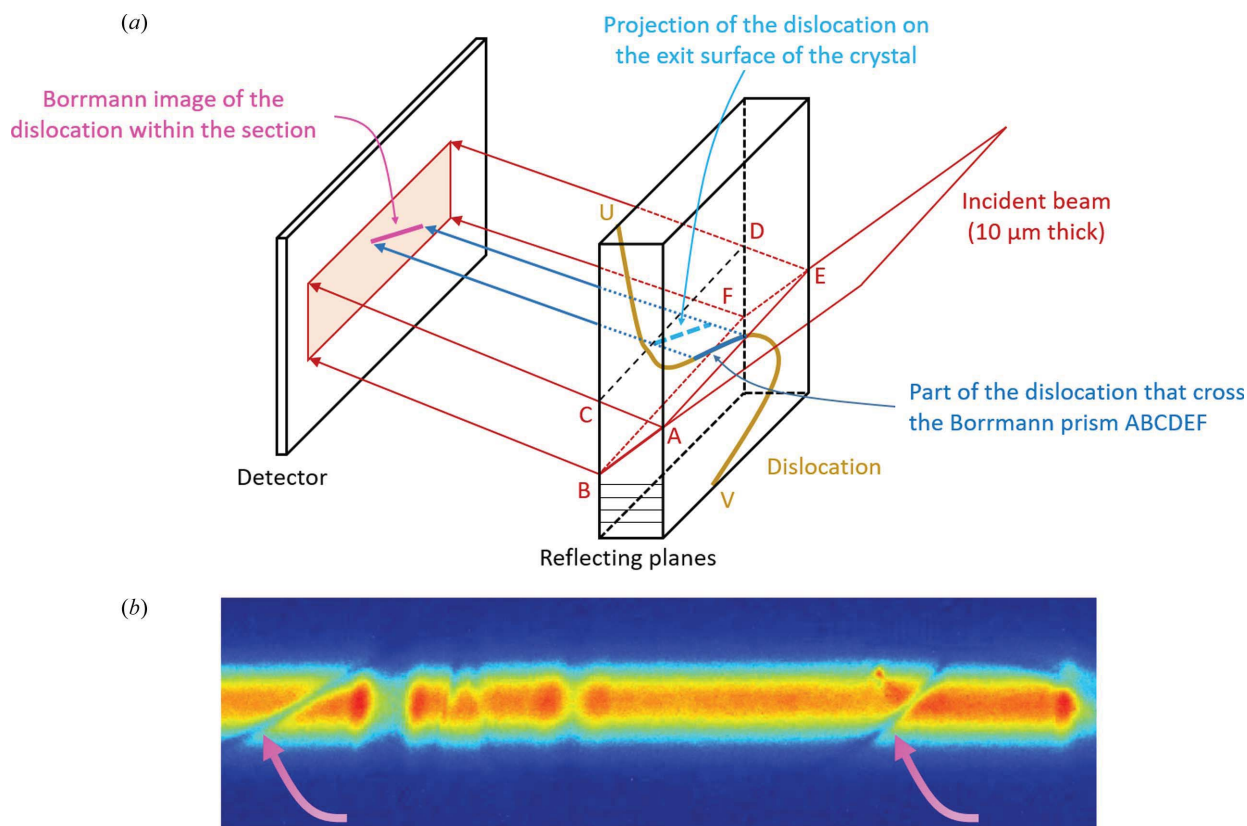
Figure 8
(*a*) Drawing highlighting (in pink) the centre of the Borrmann image on a section topograph of a dislocation that crosses the Borrmann prism ABCDEF. (*b*) Section topograph of the 0.5 mm-thick sample of CdTe(Zn). The pink arrows indicate the Borrmann images of the two dislocations D_1 and D_2 indicated in Fig. 2.

The images of the dislocations are, as expected, portions of lines (and not a dot, as is common when the absorption is small and the interference fringes are averaged out). As the dislocations lie close to the exit surface these lines nearly go from one side to the other of the section.

References

Authier, A. (2004). *Dynamical Theory of X-ray Diffraction*. Oxford University Press.

Authier, A., Lefeld-Sosnowska, M., Epelboin, Y. & Soyer, A. (1985). *J. Appl. Cryst.* **18**, 93–105.

Baruchel, J. (1996). *X-ray and Neutron Dynamical Diffraction: Theory and Applications*, edited by A. Authier, S. Lagomarsino & B. K. Tanner, pp. 199–210. Boston: Springer US.

Basson, J. H. & Booyens, H. (1983). *Phys. Status Solidi A*, **80**, 663–668.

Borrmann, G. (1941). *Phys. Z.* **42**, 157–162.

Brellier, D., Gout, E., Gaude, G., Pelenc, D., Ballet, P., Miguet, T. & Manzato, M. C. (2014). *J. Elec Mater.* **43**, 2901–2907.

Capper, P. (1994). *Properties of Narrow Gap Cadmium-Based Compounds*. London: INSPEC.

Klapper, H. (1996). *X-ray and Neutron Dynamical Diffraction: Theory and Applications*, edited by A. Authier, S. Lagomarsino & B. K. Tanner, pp. 137–146. Boston: Springer US.

Lübbert, D., Baumbach, T., Härtwig, J., Boller, E. & Pernot, E. (2000). *Nucl. Instrum. Methods Phys. Res. B*, **160**, 521–527.

Mikulík, P., Lübbert, D., Pernot, P., Helfen, L. & Baumbach, T. (2006). *Appl. Surf. Sci.* **253**, 188–193.

Sauvage, M. (1980). *Characterization of Crystal Growth Defects by X-ray Methods*, edited by B. K. Tanner & D. K. Bowen, pp. 433–455. Boston: Springer US.

Servidori, M., Cembali, F. & Milita, S. (2001). *Appl. Phys. A*, **73**, 75–82.

Suvorov, E. V. & Smirnova, I. A. (2015). *Phys.-Usp.* **58**, 833–849.

Suvorov, E. V., Smirnova, I. A. & Shulakov, E. V. (2007). *J. Surf. Investig. X-ray Synchrotron Neutron Tech.* **1**, 498–512.

Takigawa, H., Yoshikawa, M. & Maekawa, T. (1988). *J. Cryst. Growth*, **86**, 446–451.

Tanner, B. K. (1996). *X-ray and Neutron Dynamical Diffraction: Theory and Applications*, edited by A. Authier, S. Lagomarsino & B. K. Tanner, pp. 147–166. Boston: Springer US.

Tran Thi Caliste, T. N., Drouin, A., Caliste, D., Detlefs, C. & Baruchel, J. (2021). *Appl. Sci.* **11**, 9054.

Tran Thi Caliste, T. N., Guigay, J.-P., Detlefs, C. & Baruchel, J. (2023). In the press.

Tsoutsouva, M. G., Oliveira, V. A., Baruchel, J., Camel, D., Marie, B. & Lafford, T. A. (2015). *J. Appl. Cryst.* **48**, 645–654.

Williams, D. B. & Carter, C. B. (1996). *Transmission Electron Microscopy: a Textbook for Materials Science*, edited by D. B. Williams & C. B. Carter, pp. 3–17. Boston: Springer US.

Yildirim, C., Ballet, P., Santailler, J.-L., Giotta, D., Obrecht, R., Tran Thi, T. N., Baruchel, J. & Brellier, D. (2021). *J. Synchrotron Rad.* **28**, 301–308.